

COMPLEX ORGANIC MOLECULES DURING LOW-MASS STAR FORMATION: PILOT SURVEY RESULTS

KARIN I. ÖBERG

Harvard-Smithsonian Center for Astrophysics, 60 Garden Street, Cambridge, MA 02138, USA

TRISH LAUCK

University of Virginia, Charlottesville, VA 22904, USA

DAWN GRANINGER

Harvard-Smithsonian Center for Astrophysics, 60 Garden Street, Cambridge, MA 02138, USA

Draft version October 23, 2018

ABSTRACT

Complex organic molecules (COMs) are known to be abundant toward *some* low-mass young stellar objects (YSOs), but how these detections relate to typical COM abundance are not yet understood. We aim to constrain the frequency distribution of COMs during low-mass star formation, beginning with this pilot survey of COM lines toward six embedded YSOs using the IRAM 30m telescope. The sample was selected from the Spitzer *c2d* ice sample and covers a range of ice abundances. We detect multiple COMs, including CH₃CN, toward two of the YSOs, and tentatively toward a third. Abundances with respect to CH₃OH vary between 0.7 and 10%. This sample is combined with previous COM observations and upper limits to obtain a frequency distributions of CH₃CN, HCOOCH₃, CH₃OCH₃ and CH₃CHO. We find that for all molecules more than 50% of the sample have detections or upper limits of 1–10% with respect to CH₃OH. Moderate abundances of COMs thus appear common during the early stages of low-mass star formation. A larger sample is required, however, to quantify the COM distributions, as well as to constrain the origins of observed variations across the sample.^a

Subject headings: astrobiology — astrochemistry — circumstellar matter — ISM: molecules — molecular processes — stars: formation — stars: protostars

1. INTRODUCTION

Interstellar complex organic molecules or COMs¹ are the proposed starting point of an even more complex, prebiotic chemistry during star and planet formation, linking interstellar chemistry with the origins of life (Herbst & van Dishoeck 2009). Determining COM abundance patterns are important to constrain the reservoirs of organic material during the formation of stars and planetary systems, and to elucidate COM formation mechanisms. COMs were first detected in the hot cores associated with high-mass star formation (Blake et al. 1987; Helmich & van Dishoeck 1997, e.g.), but during the past decade COMs have been detected in an increasingly diverse set of environments, including pre-stellar cores, protostellar envelopes, outflows and hot cores in low-mass star forming regions (Cazaux et al. 2003; Bottinelli et al. 2004b, 2007; Arce et al. 2008; Öberg et al. 2010b, 2011b; Bacmann et al. 2012; Cernicharo et al. 2012). These detections suggest the existence of robust formation pathways of COMs, and hence that COMs might be common

during the formation of low-mass or Solar-type stars.

Based on the observed abundances of COMs and the diversity of their hosts, most complex molecules are proposed to form on the surfaces of interstellar dust grains and in icy grain mantles (Herbst & van Dishoeck 2009). Atom addition reactions on grains should be efficient at all temperatures, but may be mainly important to form smaller organics such as CH₃OH. Ice photodissociation followed by diffusion and radical-radical combination reactions in the ice should result in an efficient formation of complex molecules at slightly elevated temperatures (T>30 K) (Garrod & Herbst 2006; Herbst & van Dishoeck 2009). In this scenario, both the initial ice composition and the level of heating and UV processing should impact on the amount of complex molecules observed in a particular source. This scenario is supported by observations on that the initial ice composition is correlated with protostellar chemistry (Öberg et al. 2009; Sakai et al. 2010), and claims of a different COM abundance pattern towards low-mass and high-mass YSOs (Öberg et al. 2011a; Caselli & Ceccarelli 2012). These claims suffer from small-number-statistics, however; there are only ~10 low-mass young stellar objects with reported detections of COMs, and the abundance distributions of COMs during low-mass star formation is therefore poorly constrained.

In this paper we present the result of a six-object pilot

koberg@cfa.harvard.edu

^a Based on observations carried out with the IRAM Plateau de Bure Interferometer. IRAM is supported by INSU/CNRS (France), MPG (Germany) and IGN (Spain).

¹ for the purpose of this paper COMs are hydrogen-rich organics containing at least three heavy elements, i.e. the kind of organics typically associated with hot cores

TABLE 1
 SOURCE INFORMATION.

Source	R.A. (J2000.0)	Dec (J2000.0)	Cloud	$L_{\text{bol}}^{\text{a,b,c}}$ L_{\odot}	$M_{\text{env}}^{\text{a,b,c}}$ M_{\odot}	$\alpha_{\text{IR}}^{\text{d}}$	$N_{\text{H}_2\text{O}}^{\text{d}}$ 10^{18} cm^{-2}	$x_{\text{CH}_3\text{OH}}^{\text{d}}$ $\%N_{\text{H}_2\text{O}}$	$x_{\text{NH}_3}^{\text{e}}$ $\%N_{\text{H}_2\text{O}}$	$x_{\text{CH}_4}^{\text{f}}$ $\%N_{\text{H}_2\text{O}}$
IRAS 03235+3004	03 26 37.45	+30 15 27.9	Perseus	1.9	2.4	1.44	14[2]	4.2[1.2]	4.7[1.0]	4.3[1.4]
B1-a	03 33 16.67	+31 07 55.1	Perseus	1.3	2.8	1.87	<1.9	3.3[1.0]	<5.8	–
B1-b	03:33:20.34	31:07:21.4	Perseus	–	26	0.68	18[3]	11.2[0.7]	4.2[2.0]	3.3[0.6]
B5 IRS 1	03 47 41.61	+32 51 43.8	Perseus	4.7	4.2	0.78	2.3[0.3]	<3.7	<2.1	–
L1489 IRS	04 04 43.07	+26 18 56.4	Taurus	3.7	–	1.10	4.3[0.5]	4.9[1.5]	5.4[1.0]	3.1[0.2]
IRAS 04108+2803	04 13 54.72	+28 11 32.9	Taurus	0.62	–	0.90	2.9[0.4]	<3.5	4.3[1.0]	<10
SVS 4-5	18 29 57.59	+01 13 00.6	Serpens	38	3.5	1.26	5.7[1.1]	25[4]	4.3[2.0]	6.1[1.7]

^aPontoppidan et al. (2004), ^bHatchell et al. (2007), ^cFurlan et al. (2008), ^dBoogert et al. (2008), ^eBottinelli et al. (2010), ^fÖberg et al. (2008)

survey of COMs toward low-mass protostars using the IRAM 30m telescope. The sample is presented in §1 and the observations and data reduction are described in §2. In §3 we present an overview of the spectral line data. We determine the column densities and, where possible, excitation temperatures of CH₃OH and detected COMs. We then use these new results together with existing literature detections and upper limits of representative COMs to obtain a first estimate of the frequency distribution of COMs toward low-mass YSOs. The results are compared with models and massive YSO chemistry in §4.

2. SOURCE SAMPLE

Our sources were selected from the *c2d* (cores to disk) ice sample (Boogert et al. 2008). The *c2d* ice sample is a sub-sample of the *c2d* survey of young stellar objects (YSOs) in nearby star-forming regions, i.e. the Perseus, Taurus, Serpens, and Corona Australis molecular cloud complexes, and a number of nearby isolated dense cores (Evans et al. 2003). The spectral energy distributions of the ice sample span a range of IR spectral indices, $\alpha = (-0.25) - 2.70$, where α is defined as the slope between 2 and 24 μm . In the infrared classification scheme $\alpha > 0.3$ defines class 0/I sources (Wilking et al. 2001), which are often, but not always, associated with young, embedded YSOs.

From this sample we considered sources on the northern sky with $\alpha > 0.3$, a H₂O ice column $> 2 \times 10^{18} \text{ cm}^{-2}$, i.e. young embedded low-mass protostars. From the 19 objects that fulfill these criteria in the *c2d* ice sample, we selected six sources that sample the observed range of ice abundances, based on CH₃OH/NH₃ and CH₃OH/H₂O abundance ratios. Table 1 lists the source coordinates, bolometric luminosities, envelope masses and the IR SED indices, together with the ice abundances. B1-b, which was the target of a previous COM search, is also included in the table (Öberg et al. 2010b). Together these seven sources span H₂O ice column densities between 2 and 14×10^{18} , which can be compared with the complete *c2d* ice sample, where $N_{\text{CH}_3\text{OH}} = 0.4 - 39 \times 10^{18} \text{ cm}^{-2}$. The sources come from three different clouds, Perseus, Taurus and Serpens, and where measured the envelopes are a few solar masses and the luminosities between one and 10s of solar luminosities. $N_{\text{CH}_3\text{OH}}/N_{\text{H}_2\text{O}} = 2 - 25\%$, which is similar to the complete sample and so is range of ratios $N_{\text{CH}_3\text{OH}}/N_{\text{NH}_3} = 0.5 - 6\%$.

None of the selected sources have been searched for COMs previously, but several have been detected in CH₃OH (Öberg et al. 2009), which is known to correlate with O-bearing COMs in hot cores (Bisschop et al.

2007). In summary this is a small sample, but it has been selected to be as representative as possible from the larger *c2d* ice sample and should thus provide a first constraint on the prevalence of complex organics during the embedded phases of low-mass star formation.

3. OBSERVATIONS

IRAS 03235+3004, B1-a, B5 IRS 1, L1489 IRS, IRAS 04108+2803 and SVS 4–5 were observed with the IRAM 30m Telescope on June 12–16, 2013 using the EMIR 90 GHz receiver and the FTS backend. The two sidebands cover 93–101 GHz and 109–117 GHz at a spectral resolution of 200 kHz or $\sim 0.5\text{--}0.6 \text{ km s}^{-1}$ (Fig. 1) and with a sideband rejection of -15dB (Carter et al. 2012). This spectral set-up was selected because of the potential large number of complex organic lines at these frequencies, and the presence of the CH₃OH 2–1 ladder.

The pointing positions are listed in Table 1 and pointing was checked every 1–2 h and found to be accurate within 2–3". Focus was checked every 4 h, and generally remained stable through most of the observations, i.e. corrections of <0.4 mm. Observations were acquired using both the position switching and wobbler switching modes. The position switching mode was attempted because of possible extended emission, but was found to have severe baseline instabilities. Comparison of the wobbler and position switch spectra revealed no significant absorption in the wobbler off-position in any of the sources, hence we only used the higher-quality wobbler spectra in this paper. The total integration time in the wobbler mode was $\sim 2\text{--}5$ h for each source, under average to good summer weather conditions ($\tau = 0.1 - 0.4$), resulting in a T_{a}^* rms of 3.5–7 mK in the lower sideband. B5 IRS1 and L1489 IRS were the only two sources with an rms above 5 mK.

The spectra were reduced using CLASS (<http://www.iram.fr/IRAMFR/GILDAS>). A global baseline was fit to each 4 GHz spectral chunk using 4–7 windows. The individual scans were baseline subtracted and averaged. To convert from antenna temperature, T_{a}^* , to main beam temperature, T_{mb} , forward efficiencies and beam efficiencies of 0.95 and 0.81 were applied. The spectra were converted to rest frequency using literature source velocities, fine-tuned using the frequencies of the CH₃OH 2–1 ladder. The absolute calibration of the spectra was also checked by comparing the CH₃OH 2–1 ladder with previous observations of some of the same sources, and were found to agree within 10% (Öberg et al. 2009).

4. RESULTS

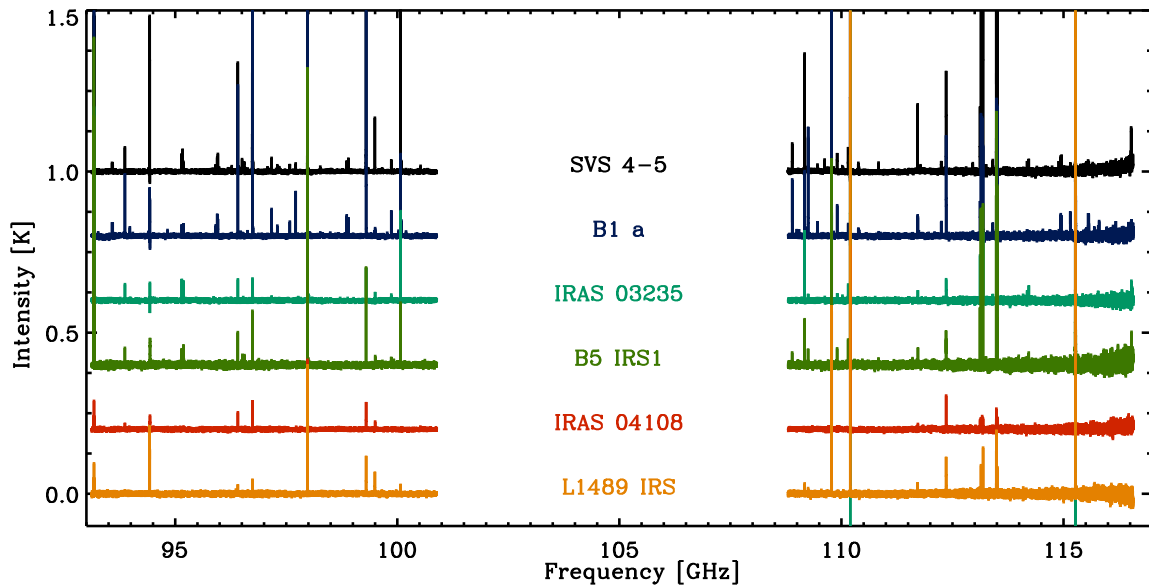


FIG. 1.— 93–101 and 109–117 GHz IRAM 30m spectra toward the LYSO sample, displaying the large variety in spectral line density between the different sources. Toward the top two sources, B1-a and SVS 4-5, many of the weak lines belong to complex organics.

4.1. Spectral analysis

Figure 1 shows the complete 16 GHz spectra toward all six sources, ordered in terms of line richness. Two of the YSOs, SVS 4-5 and B1-a, stand out as particularly line rich. Both sources are in the vicinity of two other YSOs, SMM4 and B1-b, that are known hosts of complex molecules. Of the remaining four sources, B5 IRS1 and IRAS 03235+2004 are more line dense compared to the two Taurus sources L1489 IRS and IRAS 04108+2803.

These differences in line density seems correlated with the strength of the CH_3OH 2–1 ladder as shown in Fig. 2. SVS 4-3 and B1-a both display strong CH_3OH lines, B5 IRS1 moderate ones, and IRAS 03235, IRAS 04108 and L1489 IRS very weak lines (peak intensities < 0.2 K). In addition to the 2–1 lines there are a handful of other CH_3OH lines throughout the observed frequency range with excitation energies of 6–83 K (as well as higher energy lines which are not detected toward any source). Table 2 lists the integrated line intensities or 3σ upper limits of all CH_3OH lines detected toward at least one source. The integrated intensities were determined using IDL and MPFIT to fit Gaussians to the expected line positions. The 1σ integrated line intensity uncertainties were extracted from the fit procedure and are often larger than the 1σ rms because it includes the fit uncertainty. 3σ upper limits were determined using the rms in each 4 GHz chunk and the average CH_3OH line FWHM (Table 3) for each source. Table 2 also presents the integrated line intensities of two $^{13}\text{CH}_3\text{OH}$ lines detected toward B1-a and SVS 4-5.

Figure 3 shows that in the case of SVS 4-5 (and B1-a) the multitude of weak lines hinted at in Figure 1 are to a large degree associated with the complex organic molecules HNC, H_2CCO , CH_3CHO , CH_3OCH_3 and CH_3CN . Line identifications were made using the Splatologue web tool drawing upon the CDMS and JPL spectral databases (Pickett et al. 1998; Müller et al. 2001). Other lines are identified with simple molecules, CH_3OH and carbon chains (carbon chain abundances will be the topic of a future publication).

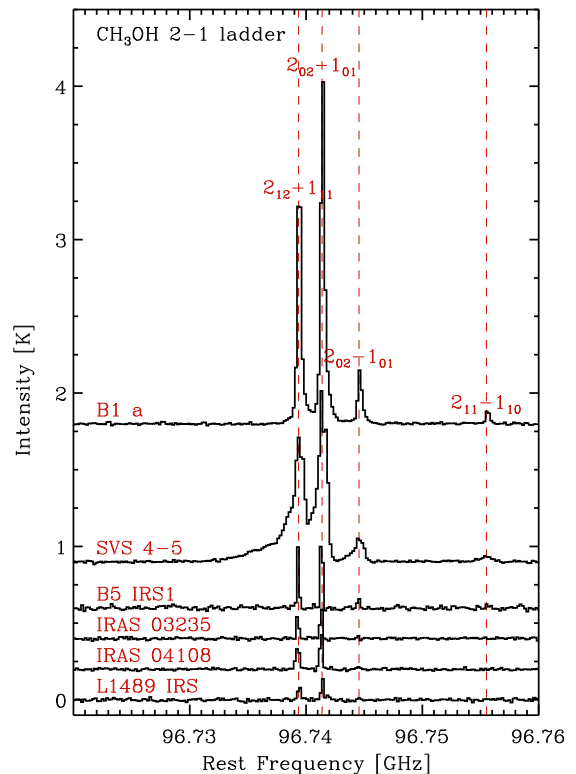


FIG. 2.— CH_3OH 2–1 spectra toward the LYSO sample displaying the order of magnitude difference in line intensities across the sample. The spectra have been shifted with the systemic velocity of each source.

Figure 4 shows blow-ups of the spectral regions with the strongest lines of the six complex organics detected toward at least one source. HNC is detected toward all sources in the sample. CH_3CHO and CH_3CN are clearly detected toward SVS 4-5 and B1-a, and marginally toward B5 IRS1. CH_3OCH_3 is only detected toward B1-a. H_2CCO is detected toward B1 a, SVS 4-5, IRAS 03235 and IRAS 04108. HCOOCH_3 is marginally detected toward SVS 4-5 and B1-a (the reality of these 3σ

TABLE 2
 INTEGRATED CH₃OH LINE INTENSITIES IN K KM S⁻¹.

Freq	QN	E _{up}	B1-a	SVS 4-5	B5 IRS1	IRAS 03235	IRAS 04108	L1489 IRS
<i>¹²CH₃OH</i>								
95.169	8 ₀₈ – 7 ₁₇	83	0.119[0.012]	0.297[0.012]	0.030[0.009]	0.016[0.011]	< 0.013	< 0.019
95.914	2 ₁₂ – 1 ₁₁	21	0.102[0.012]	0.100[0.017]	0.033[0.019]	< 0.011	0.017[0.012]	< 0.019
96.739	2 ₁₂ – 1 ₁₁	12	2.280[0.010]	3.325[0.019]	0.293[0.012]	0.161[0.006]	0.186[0.009]	0.092[0.014]
96.741	2 ₀₂ – 1 ₀₁	6	3.113[0.009]	3.272[0.015]	0.514[0.009]	0.179[0.085]	0.225[0.014]	0.116[0.010]
96.745	2 ₀₂ – 1 ₀₁	20	0.509[0.010]	0.487[0.015]	0.057[0.124]	<0.011	0.017[0.008]	<0.019
96.756	2 ₁₁ – 1 ₁₀	28	0.113[0.010]	0.138[0.018]	<0.018	<0.011	<0.013	<0.019
97.583	2 ₁₁ – 1 ₁₀	21	0.119[0.009]	0.118[0.015]	< 0.018	<0.011	<0.013	<0.019
108.894	0 ₀₀ – 1 ₁₁	13	0.437[0.011]	0.429[0.018]	0.080[0.022]	< 0.012	< 0.013	< 0.021
<i>¹³CH₃OH</i>								
94.405	2 ₁₂ – 1 ₁₁	12	0.040[0.009]	0.047[0.012]	<0.018	<0.011	<0.013	<0.019
94.407	2 ₀₂ – 1 ₀₁	7	0.052[0.0012]	0.043[0.013]	<0.018	<0.011	<0.013	<0.019

 TABLE 3
 LINE FWHM WITH STANDARD DEVIATIONS.

Source	FWHM _{CH₃OH} [km/s]
B1-a	1.6[0.4]
SVS 4-5	3.7[0.7]
B5 IRS1	0.8[0.1]
IRAS 03235	0.9[0.5]
IRAS 04108	1.2[0.6]
L1489 IRS	1.6[1.0]

detections are supported by several more marginal detections throughout the spectral range). In general we claim marginal detections for line intensities that exceed the 3σ upper limit for that source and sideband. To count as a clear detection we furthermore require that the Gaussian fit is sufficiently well-defined to result in an integrated intensity estimate of 30% or less. Table 4 lists the detected COM line intensities and upper limits, calculated using Gaussian fits as described for CH₃OH lines above.

4.2. CH₃OH and COM abundances

The CH₃OH excitation temperatures and column densities were determined using the rotational diagram method (Goldsmith & Langer 1999), assuming optically thin lines and LTE at a single temperature – the validity of these assumptions and the constraints on the kinetic temperatures provided by the excitation temperatures are explored further in §4.3. Figure 5 shows the results for CH₃OH. A single fit to all lines result in excitation temperatures of 15–20 K for the sources with any high energy lines detected.

The observed CH₃OH emission does not generally seem to be well described by a single excitation temperature, however, but rather seems to trace a warm and cold component. Too few high energy lines are detected to quantify the warm component, but the cold component excitation temperatures and column densities can be estimated by focusing on the low-energy lines for the fit. This result in excitation temperatures of 6–8 K. The derived column densities should be representative of the protostellar envelopes outside of the core region where thermal evaporation is possible, i.e. at T < 100 K – because CH₃OH is readily sub-thermally excited it is not possible to *a priori* constrain the emission region any

further. For IRAS 03235, too few low energy lines were detected to determine an envelope temperature, and an excitation temperature of 8 K was assumed to constrain the envelope column density.

To estimate the amount of warm CH₃OH column (beam-averaged) in each line of sight we use an excitation temperature of 26 K, based on the CH₃CN analysis below, and the one high-energy CH₃OH line excluded in the cold component fit. Table 5 reports the excitation temperatures and column densities calculated for the three fits characterizing the total, the cold and the warm protostellar CH₃OH column. The cold column densities range between $0.5 - 10 \times 10^{13}$ cm⁻², the warm column densities range between $< 0.12 - 9 \times 10^{13}$ cm⁻² and the total column densities range between $0.5 - 23 \times 10^{13}$ cm⁻². The column density uncertainties includes a 10% calibration uncertainty in addition to the fit uncertainty. The listed uncertainties do not incorporate the fact that the cold component will contribute slightly to the high energy line intensity and vice versa, resulting in systematic overestimates of the cold and warm component column densities, and indeed the sum of the cold+warm component column densities is 10–50% higher compared to the column densities derived from the single component fit. The component column densities are thus at best accurate within a factor of 2.

Figure 6 shows that CH₃CHO and CH₃CN line intensities can be fit by a single excitation temperature. Based on this analysis, CH₃CHO is characterized by a low excitation temperature (8–9 K) consistent with the CH₃OH cold component. This does not rule out the existence of a warm CH₃CHO component, since upper limits of higher energy lines are inconclusive, but the detected CH₃CHO does not originate in a hot core. In contrast the CH₃CN excitation temperature of 26 K is suggestive of a warm, possibly a hot core, origin for CH₃CN. The HCOOCH₃ detections have low SNR and also a small spread in energy levels and the derived excitation temperatures of 7–8 K are therefore highly uncertain. For CH₃OH as well as these COMs, the derived excitation temperatures depend on the kinetic temperatures. The two temperatures are rarely identical, however, and the relationship between them depend on the details of the excitation conditions and molecular excitation properties. In the case of CH₃CHO, CH₃CN and CH₃OH, comparable dipole moments, result in that the relative excitation temperatures constrain the relative excitation conditions of the

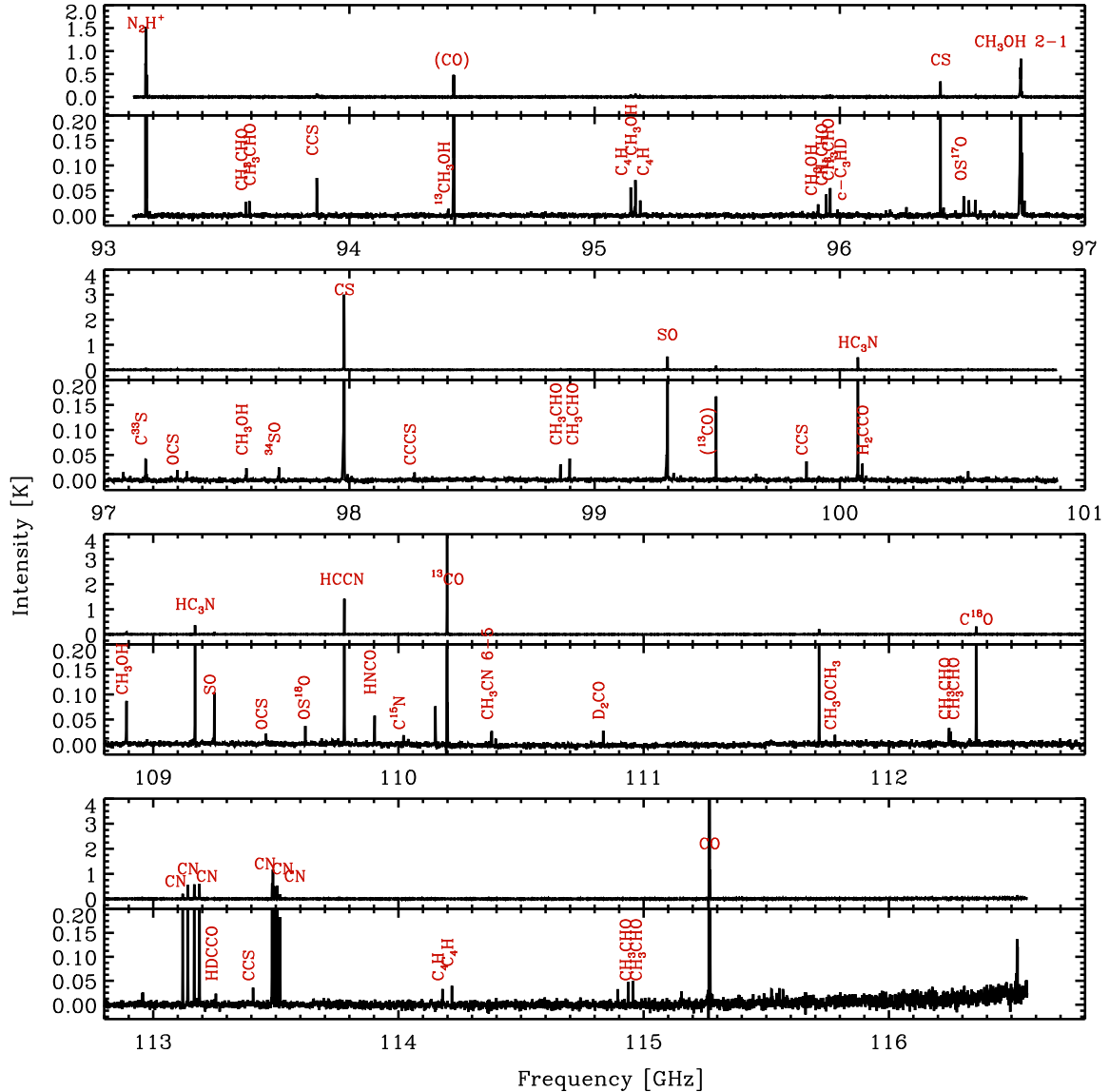


FIG. 3.— Spectra at 93–101 and 109–117 GHz toward SVS 4–5 with key lines identified. For each 4 GHz frequency chunk a zoom-out and zoomed-in view is shown to visualize the range of line strengths, and the presence of both simple and more complex molecules in this frequency range. Notable identifications are CH_3OH , CH_3CHO , CH_3OCH_3 , H_2CCO , HNCO and CH_3CN . Note that CO and ^{13}CO both presents line ‘ghosts’ in the lower sideband spectrum.

different molecules, i.e. CH_3CN is more centrally peaked compared to CH_3CHO (*cf.* §4.3), even though the specific emission locations of the different molecules are unconstrained.

Table 6 lists the resulting excitation temperatures and beam-averaged column densities, i.e. the reported column densities do not take into account potential beam dilution, which may be substantial for some or all molecules. For the detected complex organic molecules, where it is not possible to determine an excitation temperature we picked a temperature, 8, 18 or 26 K, based on recent observations of spatial and excitation temperature correlations of different molecules around high-mass protostars (Bisschop et al. 2007; Öberg et al. 2013, Fayolle et al. subm. ApJ). In these studies H_2CCO and CH_3CHO are cold and we therefore used the CH_3CHO excitation temperature of 8 K to determine the H_2CCO column. CH_3OCH_3 and CH_3CN emission were gener-

ally associated with only warm material and we used the CH_3CN excitation temperature of 26 K to determine the CH_3OCH_3 column. HNCO , like CH_3OH , has been observed to trace both cold and warm material and we therefore used an excitation temperature of 18 K, typical for the CH_3OH when fitting a single LTE component to the protostellar data. It is important to note that the excitation temperature choices are based on a small set of high-mass protostellar data and may need to be revised once more spatially resolved observations of complex molecules toward low-mass protostars exist.

We used the derived complex molecule column densities together with the derived CH_3OH column densities to calculate the abundances of organic molecules with respect to CH_3OH in our source sample. We tested the sensitivity of the derived abundances on the selected CH_3OH components for different molecules, and generally found that the choice of excitation temperature and

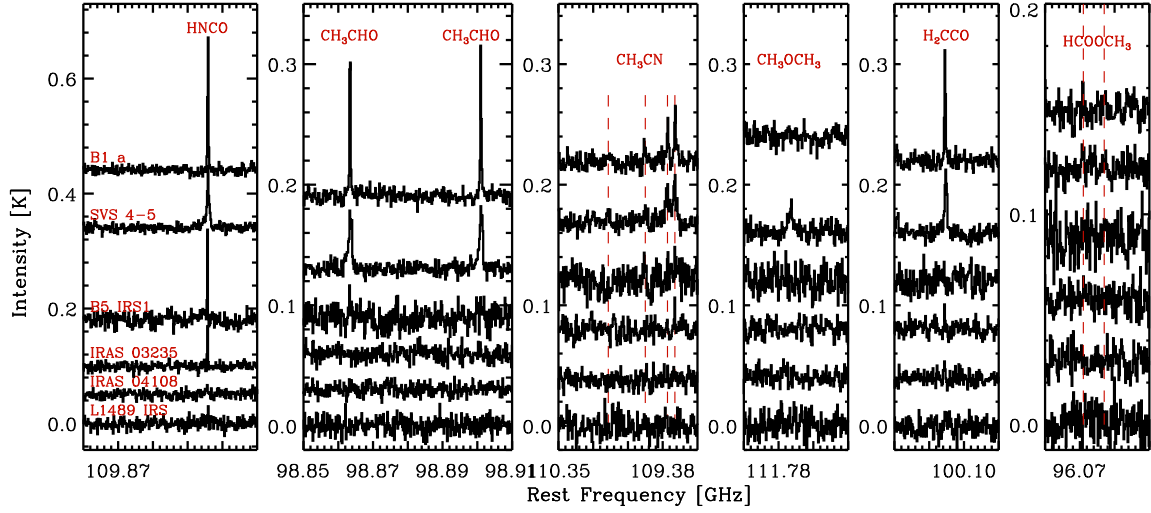


FIG. 4.— Zoomed in spectra of HNCO, CH₃CHO, CH₃CN, CH₃OCH₃, H₂CCO and HCOOCH₃, toward the LYSO sample. All spectra have been shifted by the source systemic velocities.

TABLE 4
INTEGRATED LINE INTENSITIES IN K KM S⁻¹ OF COMPLEX ORGANIC MOLECULES.

Freq	E _{up}	B1-a	SVS 4-5	B5 IRS1	IRAS 03235	IRAS 04108	L1489 IRS
<i>HNCO</i>							
109.906	15	0.220[0.009]	0.200[0.013]	0.106[0.019]	0.050[0.008]	0.031[0.014]	0.027[0.007]
<i>H₂CCO</i>							
100.095	27	0.110[0.008]	0.099[0.011]	<0.011	0.020[0.012]	0.027[0.010]	<0.017
<i>CH₃CN</i>							
110.375	47	0.018[0.006]	0.017[0.011]	0.031[0.011]	< 0.012	< 0.013	< 0.02
110.381	25	0.046[0.011]	0.073[0.015]	0.024[0.008]	< 0.012	< 0.013	< 0.021
110.383	18	0.062[0.011]	0.085[0.015]	0.020[0.007]	< 0.012	< 0.013	< 0.021
<i>CH₃CHO</i>							
93.581	15	0.098[0.008]	0.115[0.015]	0.016[0.008]	< 0.011	< 0.013	< 0.019
93.595	15	0.106[0.010]	0.125[0.014]	<0.018	< 0.011	< 0.013	< 0.019
95.947	13	0.161[0.007]	0.204[0.014]	<0.018	< 0.011	< 0.013	< 0.019
95.963	13	0.176[0.008]	0.204[0.014]	<0.018	< 0.011	< 0.013	< 0.019
96.274	22	0.042[0.009]	0.061[0.014]	<0.018	< 0.011	< 0.013	< 0.019
96.426	22	0.033[0.009]	0.065[0.013]	<0.016	< 0.010	< 0.011	< 0.017
96.476	23	0.043[0.010]	0.045[0.014]	<0.016	< 0.010	< 0.011	< 0.017
96.633	22	0.050[0.009]	0.039[0.013]	<0.016	< 0.010	< 0.011	< 0.017
98.863	16	0.155[0.009]	0.162[0.014]	0.021[0.006]	< 0.010	< 0.011	< 0.017
98.901	16	0.138[0.007]	0.168[0.013]	0.041[0.015]	< 0.010	< 0.011	< 0.017
112.249	21	0.096[0.010]	0.131[0.016]	0.015[0.008]	< 0.012	< 0.013	< 0.021
112.255	21	0.107[0.009]	0.149[0.019]	0.032[0.021]	< 0.012	< 0.013	< 0.021
<i>CH₃OCH₃</i>							
111.783	25	<0.013	0.085[0.019]	<0.019	< 0.012	< 0.013	< 0.021
115.545	14	<0.027	0.080[0.028]	<0.032	< 0.019	< 0.024	< 0.035
<i>HCOOCH₃</i>							
96.071	23	0.019[0.004]	0.022[0.013]	<0.018	< 0.010	< 0.011	< 0.017
96.077	23	0.018[0.011]	<0.032	<0.018	< 0.010	< 0.011	< 0.017
100.482	22	0.014[0.011]	0.023[0.010]	<0.011	< 0.010	< 0.011	< 0.017
100.491	22	0.020[0.010]	0.035[0.015]	<0.011	< 0.010	< 0.011	< 0.017
100.683	24	0.018[0.009]	0.044[0.013]	<0.011	< 0.010	< 0.011	< 0.017
111.674	28	0.022[0.013]	0.020[0.011]	<0.019	< 0.012	<0.013	< 0.021
111.682	28	0.019[0.017]	0.010[0.011]	<0.019	< 0.012	<0.013	< 0.021

TABLE 5
 CH_3OH EXCITATION TEMPERATURES AND COLUMN DENSITIES. THE LISTED UNCERTAINTIES ARE THE FORMAL ERRORS; THE SYSTEMATIC COLUMN DENSITY UNCERTAINTIES ARE ESTIMATED TO $\sim 50\%$ BASED ON LVG ANALYSIS OF B1-A.

Source	$T_{\text{rot}}^{\text{ave}}$ [K]	$N_{\text{CH}_3\text{OH}}^{\text{ave}}$ [cm^{-2}]	$T_{\text{rot}}^{\text{cold}}$ [K]	$N_{\text{CH}_3\text{OH}}^{\text{cold}}$ [cm^{-2}]	$T_{\text{rot}}^{\text{warm}^{\text{b}}}$ [K]	$N_{\text{CH}_3\text{OH}}^{\text{warm}^{\text{c}}}$ [cm^{-2}]
B1-a	14.9[0.6]	$1.3[0.2] \times 10^{14}$	5.9[0.3]	$8.4[1.9] \times 10^{13}$	(26)	$9[3] \times 10^{13}$
SVS 4-5	20.2[0.9]	$2.3[0.4] \times 10^{14}$	5.9[0.3]	$10[2] \times 10^{13}$	(26)	$2.2[0.5] \times 10^{14}$
B5 IRS1	17[2]	$4.3[0.9] \times 10^{13}$	8[1]	$2.1[0.7] \times 10^{13}$	(26)	$2.3[1.2] \times 10^{13}$
IRAS 03235	18[4]	$2.8[0.9] \times 10^{13}$	(8) ^a	$1.1[0.5] \times 10^{13}$	(26)	$1.2[1.1] \times 10^{13}$
IRAS 04108	9[3]	$1.2[0.5] \times 10^{13}$	9[3]	$1.2[0.5] \times 10^{13}$	(26)	$< 8 \times 10^{12}$
L1489 IRS	8[4]	$5[5] \times 10^{12}$	8[4]	$5[5] \times 10^{12}$	(26)	$< 1.3 \times 10^{12}$

^aNo excitation temperature could be independently derived and the sample average of 8 K was assumed.

^b26 K is the assumed excitation temperature for the warm CH_3OH component.

^cBased on the intensity or upper limit of the CH_3OH 95.169 GHz line.

TABLE 6
 COMPLEX MOLECULE EXCITATION TEMPERATURES AND COLUMN DENSITIES.

Source	CH_3CHO		CH_3CN		HCOOCH_3		HNCO^{b}	$\text{H}_2\text{CCO}^{\text{b}}$	$\text{CH}_3\text{OCH}_3^{\text{b}}$
	$T_{\text{rot}}^{\text{a}}$ [K]	N [cm^{-2}]	$T_{\text{rot}}^{\text{a}}$ [K]	N [cm^{-2}]	$T_{\text{rot}}^{\text{a}}$ [K]	N [cm^{-2}]	N ($T_{\text{rot}} = 18 \text{ K}$) [cm^{-2}]	N ($T_{\text{rot}} = 8 \text{ K}$) [cm^{-2}]	N ($T_{\text{rot}} = 26 \text{ K}$) [cm^{-2}]
B1-a	8[1]	$6[2] \times 10^{12}$	26[8]	$1.2[0.6] \times 10^{12}$	7[7]	$9[26] \times 10^{12}$	$2.6[0.3] \times 10^{12}$	$6.8[1.2] \times 10^{12}$	$< 6 \times 10^{12}$
SVS 4-5	9[2]	$7[2] \times 10^{12}$	26[9]	$1.7[0.9] \times 10^{12}$	8[9]	$1[3] \times 10^{13}$	$2.4[0.4] \times 10^{12}$	$5.9[1.3] \times 10^{12}$	$2.2[1.0] \times 10^{13}$
B5 IRS1	(8)	$1.9[0.7] \times 10^{12}$	(26)	$4[2] \times 10^{11}$	(8)	$< 4 \times 10^{12}$	$1.2[0.4] \times 10^{12}$	$< 9 \times 10^{11}$	$< 8 \times 10^{12}$
IRAS 03235	(8)	$< 7 \times 10^{11}$	(26)	$< 3 \times 10^{11}$	(8)	$< 2 \times 10^{12}$	$6.0[1.6] \times 10^{11}$	$1.2[0.8] \times 10^{12}$	$< 5 \times 10^{12}$
IRAS 04108	(8)	$< 6 \times 10^{11}$	(26)	$< 4 \times 10^{11}$	(8)	$< 1 \times 10^{12}$	$4[2] \times 10^{11}$	$1.6[0.9] \times 10^{12}$	$8[4] \times 10^{12}$
L1489 IRS	(8)	$< 1.0 \times 10^{12}$	(26)	$< 6 \times 10^{11}$	(8)	$< 2 \times 10^{12}$	$3.2[1.1] \times 10^{11}$	$2.5[1.1] \times 10^{12}$	$< 8 \times 10^{12}$

^a(T) is used to indicate that the sample average excitation temperature was used to derive a column density or upper limit.

^bThe average CH_3OH , CH_3CHO and CH_3CN excitation temperatures were used to derive the HNCO , H_2CCO and CH_3OCH_3 column densities, respectively.

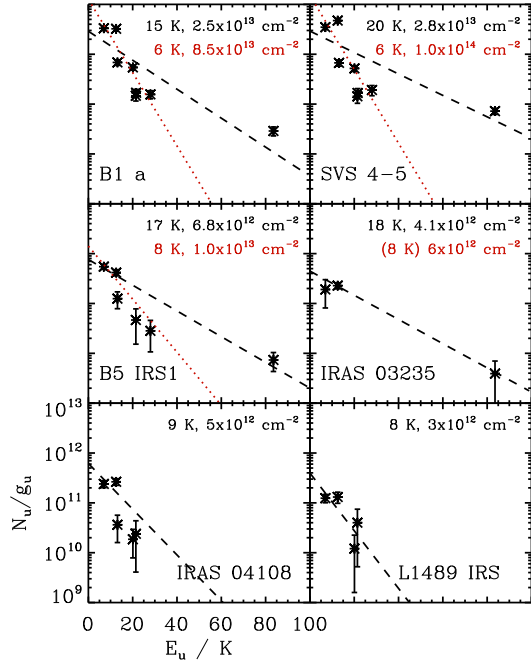


FIG. 5.— CH_3OH rotational diagrams. Black lines and labels are for the fit to all lines. Red lines and labels are for fits that exclude high-energy lines.

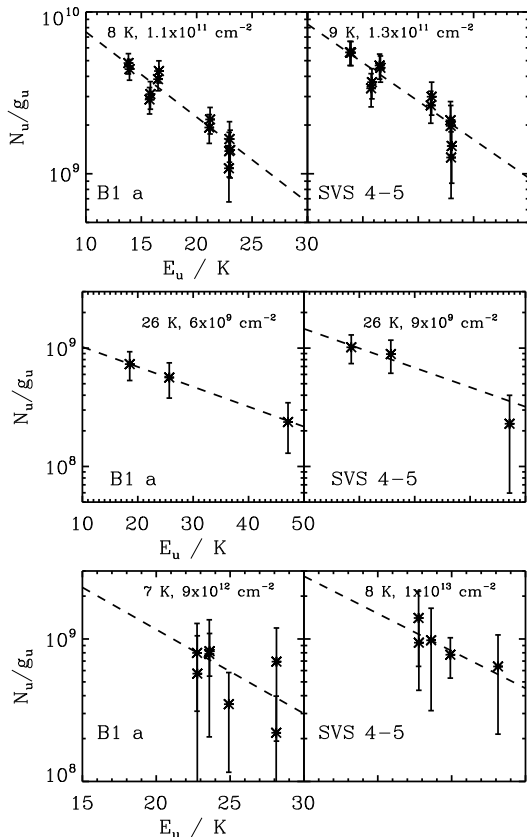


FIG. 6.— CH_3CHO (top), CH_3CN (middle), and HCOOCH_3 (bottom) rotational diagrams.

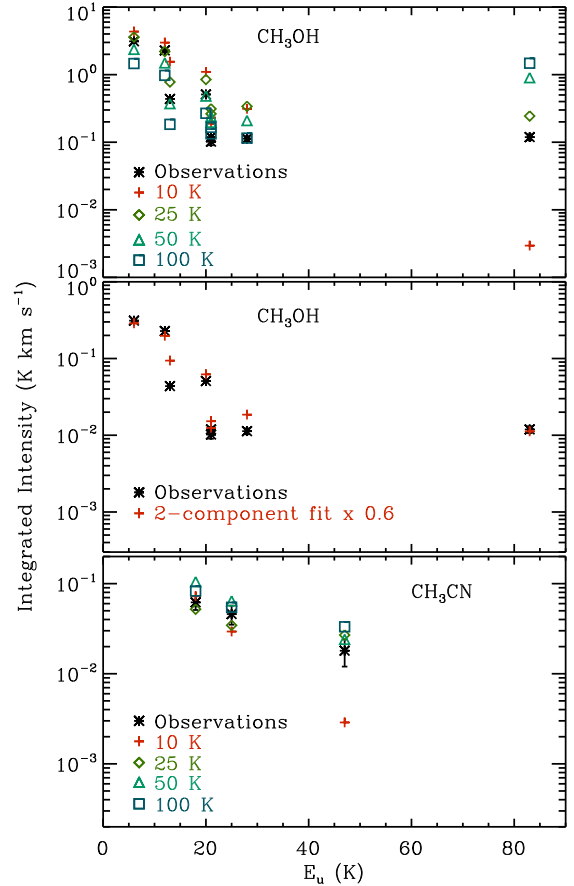


FIG. 7.— Comparisons between observed and modeled line intensities toward B1-a using RADEX. The top panel show CH_3OH lines and models assuming a single component with constant temperature, a density of 10^6 cm^{-3} , and the derived average column from the rotational diagram analysis. The middle panel compares the same data with a two component fit, using the temperatures of the cold and warm component in Table 5, but multiplying the column densities by 0.6. The bottom panel compares the observed and model CH_3CN line intensities.

CH_3OH reference column density (beam-averaged, cold or warm components) affected the derived abundances with respect to CH_3OH by less than a factor of 2. Table 7 shows that the CH_3CHO abundances are between 7 and 9% and the upper limits between 5 and 20% with respect to CH_3OH . CH_3CN and CH_3OCH_3 abundances or upper limits could only be derived toward the first four sources since no lines associated with warm CH_3OH were detected toward two of the sources. The CH_3CN abundances are 0.8–1.7% and the CH_3OCH_3 abundance toward SVS 4-5 is 10%. The HCOOCH_3 abundances are $\sim 10\%$, but abundances up to 40% cannot be excluded. The HNCO abundances vary between 1.0–6.4%, and the H_2CCO abundances vary between 1.1–9%. Derived upper limits are typically similar or higher compared to detections.

4.3. Optical depth and LVG modeling

The analysis in the previous section assumes that all observed complex organic emission is optically thin. This is a tenuous assumption for CH_3OH , since CH_3OH lines are known to sometimes be optically thick toward protostars (e.g. Bisschop et al. 2007). Fortunately, the $^{13}\text{CH}_3\text{OH}$ 2–1 ladder falls within the observed frequency

TABLE 7
COMPLEX MOLECULE ABUNDANCES WITH RESPECT TO CH₃OH IN %.

Source	x _{CH₃CHO}	x _{CH₃CN}	x _{HNCO}	x _{H₂CCO}	x _{CH₃OCH₃}	x _{HCOOCH₃}
B1-a	7[3]	1.3[0.8]	2.0[0.4]	1.4[0.3]	<7	11[19]
SVS 4-5	7[2]	0.8[0.4]	1.0[0.3]	1.1[0.2]	10[5]	10[30]
B5 IRS1	9[4]	1.7[1.3]	2.8[1.1]	<0.8	<35	<21
IRAS 03235	<6	<2.5	2.1[0.9]	2.0[1.5]	<42	<15
IRAS 04108	<5	- ^a	3.3[2.2]	2.4[1.4]	- ^a	<12
L1489 IRS	<20	- ^a	6.4[6.7]	9[9]	- ^a	<46

^aNo upper limit could be derived because of lack of detection of warm CH₃OH.

range, enabling a direct test of this assumption. Two ¹³CH₃OH lines are detected toward B1-a and SVS 4-5, but not toward any other sources. The line intensity ratios between corresponding CH₃OH and ¹³CH₃OH lines are 57–60[15] and 71–76[19] toward B1-a and SVS 4–5, respectively, consistent with the Solar ¹²C/¹³C ratio of 77. CH₃OH, and by inference all other COM, emission lines thus appear to be optically thin.

A second question is how the excitation temperatures, derived using rotational diagrams, relate to the kinetic temperatures in the emission regions. To explore this, we carried out a Large Velocity Gradient (LVG) radiative transfer analysis using RADEX (van der Tak et al. 2007) for the molecules with both sufficient number of lines to constrain the excitation conditions and known collision cross sections, i.e. CH₃OH and CH₃CN, toward B1-a. B1-a is here taken to be representative of the sample because of the similar emission patterns of CH₃OH and CH₃CN (when detected) across the sample (Figs. 5–6).

We ran a grid of RADEX models with $n_{\text{H}} = [10^5, 10^6]$ cm⁻³, $T_{\text{kin}} = [10, 25, 50, 100]$ K, and CH₃OH and CH₃CN column densities ranging between 0.5× and 2× those listed in Tables 2–4 for B1-a. The models with a factor of 2 lower and higher column densities compared to the rotational diagram values cannot be excluded for all temperatures and densities, but generally fit the data less well. This indicates that the rotational diagram method provides a good estimate of the beam-averaged column densities, but that the real uncertainty in the derived numbers are at least a factor of two rather than the formal uncertainties of 20–50%.

Figure 7 shows the model results for the best fit column densities (i.e. the ones derived using the rotational diagram method), and a density of 10⁶ cm⁻³. The best fit temperature to the CH₃OH data, assuming a single component, is between 10 and 25 K, consistent with the rotational diagram excitation temperature. If a lower density of 10⁵ cm⁻² is assumed, kinetic temperatures up to 50 K fit the data. However, such a low average density is unlikely based on Jørgensen et al. (2002), where a detailed envelope modeling shows that the average density toward deeply embedded protostars on 1000 AU scales is $\sim 10^6$ cm⁻³. In either case, it can be excluded that most of the CH₃OH emission originates in a hot core. As in the rotational diagram analysis, no single temperature component fits all the CH₃OH lines. The two components derived in Table 5 reproduces the relative line intensities very well, but over-predicts the line intensities by about 50% as discussed above. In the case of CH₃CN, only kinetic temperatures of 25 K and higher are consistent with the data, confirming the rotational diagram results that

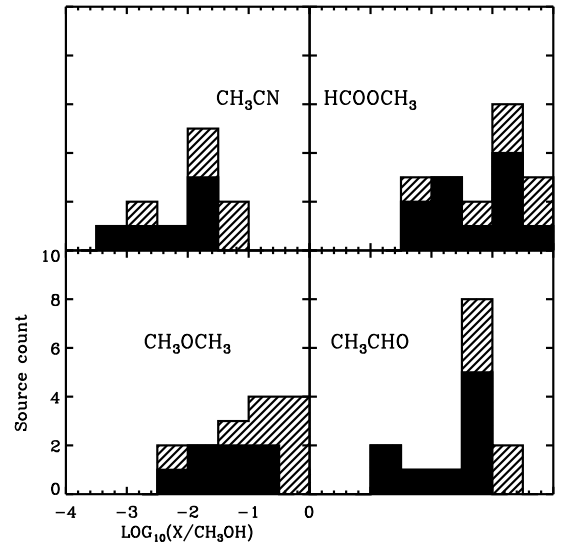


FIG. 8.— Histograms of the abundances of selected complex organics with respect to CH₃OH taken from our sample and the literature. The solid bars are detections and line-filled bars indicated upper limits.

CH₃CN has of a more centrally peaked origin compared to CH₃OH.

In summary, the analyzed emission lines are optically thin and the rotational diagram method provides an accurate (within a factor of 2) derivation of the molecular column densities. The excitation temperatures and the kinetic temperatures are not identical, but the observed difference in excitation temperatures for CH₃CN and CH₃OH corresponds to a real difference in kinetic temperatures for reasonable density assumptions.

4.4. Sample statistics

In addition to the low-mass young stellar objects presented here, CH₃CHO, HCOOCH₃, CH₃CN, and/or CH₃OCH₃ have been previously quantified toward B1-b in Perseus (Öberg et al. 2009, 2010a), SMM1, SMM4 and SMM4-W in Serpens (Öberg et al. 2011b), L1157 (Arce et al. 2008), NGC 1333 IRAS 2A, 4A and 4B in Perseus (Bottinelli et al. 2004a, 2007), and toward IRAS 16293-2422, both including the binary in one beam, and toward the A and B cores separately (Cazaux et al. 2003; Bisschop et al. 2008). The abundance frequency histograms with respect to CH₃OH are shown in Fig. 8 for the combined low-mass sample of literature sources and our six YSOs. Complex molecule abundances above 1% are clearly common. The median detected abundances for the four species HCOOCH₃, CH₃CHO, CH₃OCH₃ and CH₃CN varies between 1% (CH₃CN) and

TABLE 8
 MEDIAN COM ABUNDANCES IN LYSOs AND MASSIVE YSOs WITH
 AND WITHOUT HOT CORES

Abundance %CH ₃ OH	LYSOs	Hot Cores ^a	MYSOs ^b
CH ₃ CN	1	7	3
HCOOCH ₃	5	12	–
CH ₃ OCH ₃	5	16	4
CH ₃ CHO	3	0.1	3

^aBisschop et al. (2007), ^bMYSOs without bright Hot Cores from Fayolle et al. (subm)

5% (HCOOCH₃ and CH₃OCH₃) with respect to CH₃OH. It is important to note that most upper limits seems to be consistent with these values and thus that the lack of complex molecules in half of our sources is most likely due to an overall low CH₃OH abundance or a low overall ice desorption rate rather than a significantly different chemistry with respect to CH₃OH.

Figure 8 also shows that the COM abundances vary significantly between sources. Disregarding upper limits CH₃CN/CH₃OH = 0.07–1.7%, HCOOCH₃/CH₃OH = 0.6–56%, CH₃OCH₃/CH₃OH = 0.8–20% and CH₃CHO/CH₃OH = 0.1–9%. For all molecules there is thus a one or two order of magnitude variation across the sample.

5. DISCUSSION

The median abundances derived from the combined low-mass YSO sample can be compared both with the more well-studied high-mass YSO chemistry and with model predictions. In a sample of seven hot cores observed by Bisschop et al. (2007) the median abundances of CH₃CN, HCOOCH₃, CH₃OCH₃ and CH₃CHO with respect to CH₃OH were 7%, 12%, 16% and 0.1%, respectively. That is, all abundances except for CH₃CHO are a factor of a few higher toward the high-mass hot cores. This may not be representative of massive YSO chemistry; in a recent sample of three high-mass YSOs without hot cores, the median abundances of CH₃CN, CH₃OCH₃ and CH₃CHO with respect to CH₃OH were all 3–4% (Fayolle et al. ApJ subm.). These abundances are quite similar to our low-mass sample. There is thus no clear observational evidence for an intrinsic difference between low-mass and high-mass YSO COM chemistry with respect to CH₃OH, when averaged over all early stages of star formation. This does not exclude that there are significant differences when comparing low-mass and high-mass objects that are at the same evolutionary stage, i.e. there may still be real differences between high-mass hot cores and their low-mass equivalents because of e.g. different protostellar collapse time scales (Garrod et al. 2008). More spatially resolved studies of low-mass YSOs are required, however, to support or reject that proposition.

This study also shows that there are orders of magnitude differences in COM abundances with respect to CH₃OH among low-mass YSOs. Three potential sources of variation are the initial ice composition, temperature and density structures and thus excitation conditions, and the chemical evolutionary stage. A unique feature of this sample is that the ice compositions are known and its relationship to the Com chemistry can thus be evaluated. There is some correlation between CH₃OH

ice and gas abundances among the 7 ice sources in Table 2, but there are also clear exceptions to this relationship, e.g. B1-a, which has a small CH₃OH ice abundance and a fairly high gas-phase abundance with respect to H₂O ice. There are no obvious correlations between the ice compositions and COM abundance patterns, in particular there is no correlation between NH₃/CH₃OH in the ice and N- and O-bearing complex molecules in the gas. This does not rule out that the ice composition is important for the complex chemistry, but in this small sample, ice composition is clearly not the dominant regulator of the observed COM chemistry.

In terms of evolutionary stage, the sample can be coarsely divided into ice sources (our sample + B1 b), embedded protostars without significant ice absorption (SMM 1, 4, and 4-W, NGC 1333 IRAS 2A, 4A and 4B, and IRAS 16293-2422), and an outflow (L1157). B1-b should potentially be in its own grouping since the COM emission seems more associated with the pre-stellar core than with the protostar. There is no significant difference between the ice sources and ice-free protostars in terms of COM emission, i.e. the median abundances within our sample are consistent with those of the ice-free protostars. The difference in envelope structure and/or evolutionary stage between these two source types thus also fails to explain the observed COM abundance variation across the sample.

Finally, assessing the importance of different excitation conditions is complicated by sparse information on the spatial origins of the complex molecule emission in the different sources. In the literature one out of two simplified distributions of COMs toward protostars is typically assumed: either that the CH₃OH and COM spatial distributions are the same and characterized by a single CH₃OH excitation temperature (e.g. Öberg et al. 2011a), or that the COM spatial distribution is more compact compared to CH₃OH (e.g. Bottinelli et al. 2007). In the latter case COM/CH₃OH abundances are calculated based on modeled CH₃OH core abundances and the assumption that all COM emission originates in the core. In this study we use the CH₃OH data to estimate the amount of cold CH₃OH in the envelope and warm CH₃OH in the core and then calculate COM/CH₃OH abundances using the cold or warm CH₃OH component or the total beam-averaged column density dependent on COM excitation temperatures and/or spatial distribution constraints from previous studies. This is a crude approximation and until spatially resolved observations of both CH₃OH and COMs exists toward a sample of low-mass YSOs, the reported abundances are estimated to be accurate only within a factor of a few, i.e. considerably less accurate than the ~30–50% uncertainties reported in Table 7 when only taking into account fit and calibration errors. There is clearly a need both to increase the existing number of sources searched for complex organics and to constrain the spatial distribution of COMs toward a sub-sample of representative sources to elucidate what source characteristics that set the observed COM abundances.

6. CONCLUSIONS

We have carried out a small, pilot survey of complex molecules in a sample of low-mass YSOs, which were selected based on their measured ice abundances in the

envelope. The results of this survey have been combined with literature values on complex molecule detections and upper limits to obtain first constraints on the abundance median and variability of complex molecule abundances during low-mass star formation. Based on this we have found:

1. Complex organics (CH_3CHO , HCOOCH_3 , CH_3OCH_3 and/or CH_3CN) are detected toward 2–3/6 embedded protostars at abundances of 0.8–11% with respect to CH_3OH (i.e. COMs are clearly detected toward two sources and marginally toward a third). Upper limits in the remaining sources are consistent with the detected abundances with respect to CH_3OH , indicative that complex molecule formation at the 1–10% level with respect to CH_3OH is common during the early stages of low-mass star formation.
2. Two other slightly less complex organic molecules, HNCO and H_2CCO are more common, and are

clearly detected in 4–6 sources in the sample.

3. When the pilot survey is combined with 8 deep searches for complex organics in the literature we obtain median values with respect to CH_3OH of 1% for CH_3CN , 3% for CH_3CHO , 5% for CH_3OCH_3 , and 5% for HCOOCH_3 for low-mass YSOs.
4. There is at least an order of magnitude variability in abundances with respect to CH_3OH for all species, but the current sample is too small and heterogeneous to constrain the origin of this variability to initial conditions, chemical evolution, or physical structures, or a combination of all three.

Acknowledgements: We gratefully acknowledge the IRAM staff for help provided during the observations and data reduction.

REFERENCES

- Arce, H. G., Santiago-García, J., Jørgensen, J. K., Tafalla, M., & Bachiller, R. 2008, *ApJ*, 681, L21
- Bacmann, A., Taquet, V., Faure, A., Kahane, C., & Ceccarelli, C. 2012, *A&A*, 541, L12
- Bisschop, S. E., Jørgensen, J. K., Bourke, T. L., Bottinelli, S., & van Dishoeck, E. F. 2008, *A&A*, 488, 959
- Bisschop, S. E., Jørgensen, J. K., van Dishoeck, E. F., & de Wachter, E. B. M. 2007, *A&A*, 465, 913
- Blake, G. A., Sutton, E. C., Masson, C. R., & Phillips, T. G. 1987, *ApJ*, 315, 621
- Boogert, A. C. A., Pontoppidan, K. M., Knez, C., et al. 2008, *ApJ*, 678, 985
- Bottinelli, S., Boogert, A. C. A., Bouwman, J., et al. 2010, *ApJ*, 718, 1100
- Bottinelli, S., Ceccarelli, C., Lefloch, B., et al. 2004a, *ApJ*, 615, 354
- Bottinelli, S., Ceccarelli, C., Neri, R., et al. 2004b, *ApJ*, 617, L69
- Bottinelli, S., Ceccarelli, C., Williams, J. P., & Lefloch, B. 2007, *A&A*, 463, 601
- Carter, M., Lazareff, B., Maier, D., et al. 2012, *A&A*, 538, A89
- Caselli, P. & Ceccarelli, C. 2012, *A&A Rev.*, 20, 56
- Cazaux, S., Tielens, A. G. G. M., Ceccarelli, C., et al. 2003, *ApJ*, 593, L51
- Cernicharo, J., Marcelino, N., Roueff, E., et al. 2012, *ApJ*, 759, L43
- Evans, II, N. J., Allen, L. E., Blake, G. A., et al. 2003, *PASP*, 115, 965
- Furlan, E., McClure, M., Calvet, N., et al. 2008, *ApJS*, 176, 184
- Garrod, R. T. & Herbst, E. 2006, *A&A*, 457, 927
- Garrod, R. T., Weaver, S. L. W., & Herbst, E. 2008, *ApJ*, 682, 283
- Goldsmith, P. F. & Langer, W. D. 1999, *ApJ*, 517, 209
- Hatchell, J., Fuller, G. A., Richer, J. S., Harries, T. J., & Ladd, E. F. 2007, *A&A*, 468, 1009
- Helmich, F. P. & van Dishoeck, E. F. 1997, *A&AS*, 124, 205
- Herbst, E. & van Dishoeck, E. F. 2009, *ARA&A*, 47, 427
- Jørgensen, J. K., Schöier, F. L., & van Dishoeck, E. F. 2002, *A&A*, 389, 908
- Müller, H. S. P., Thorwirth, S., Roth, D. A., & Winnewisser, G. 2001, *A&A*, 370, L49
- Öberg, K. I., Boamah, M. D., Fayolle, E. C., et al. 2013, *ApJ*, 771, 95
- Öberg, K. I., Boogert, A. C. A., Pontoppidan, K. M., et al. 2008, *ApJ*, 678, 1032
- Öberg, K. I., Boogert, A. C. A., Pontoppidan, K. M., et al. 2011a, *ApJ*, 740, 109
- Öberg, K. I., Bottinelli, S., Jørgensen, J. K., & van Dishoeck, E. F. 2010a, *ApJ*, 716, 825
- Öberg, K. I., Bottinelli, S., & van Dishoeck, E. F. 2009, *A&A*, 494, L13
- Öberg, K. I., Qi, C., Fogel, J. K. J., et al. 2010b, *ApJ*, 720, 480
- Öberg, K. I., van der Marel, N., Kristensen, L. E., & van Dishoeck, E. F. 2011b, *ApJ*, 740, 14
- Pickett, H. M., Poynter, R. L., Cohen, E. A., et al. 1998, *J. Quant. Spec. Radiat. Transf.*, 60, 883
- Pontoppidan, K. M., van Dishoeck, E. F., & Dartois, E. 2004, *A&A*, 426, 925
- Sakai, N., Sakai, T., Hirota, T., & Yamamoto, S. 2010, *ApJ*, 722, 1633
- van der Tak, F. F. S., Black, J. H., Schöier, F. L., Jansen, D. J., & van Dishoeck, E. F. 2007, *A&A*, 468, 627
- Wilking, B. A., Bontemps, S., Schuler, R. E., Greene, T. P., & André, P. 2001, *ApJ*, 551, 357